

PdAg Bimetallic Nanoparticles Encapsulated in Porous Carbon Derived from UIO-66 as Electrocatalyst for Oxygen Reduction and Hydrogen Evolution Reactions

Wei He^{1,*}, Xiaoqing Li¹, Zhengxin Qian^{2,3}, Zhen Liu⁴, and Zhenghua Tang^{3,*}

¹ Chongqing Chemical Industry Vocational College, Chongqing, 401220, P. R. China

² School of Pharmacy, Guangdong Pharmaceutical University, Guangzhou, 510006, P. R. China.

³ Guangzhou Key Laboratory for Surface Chemistry of Energy Materials, New Energy Research Institute, School of Environment and Energy, South China University of Technology, Guangzhou Higher Education Mega Centre, Guangzhou, 510006, China.

⁴ Department of Physics & Engineering, Frostburg State University, Frostburg, MD 21532-2303, United States.

*E-mail: hewei644000@163.com, zhht@scut.edu.cn

Received: 2 April 2019 / Accepted: 19 June 2019 / Published: 31 July 2019

Developing dual functional electrocatalyst for both oxygen reduction reaction (ORR) and hydrogen evolution reaction (HER) is critical for promoting energy conversion efficiency in fuel cells and metal-air batteries, and produce hydrogen with high purity. Herein, PdAg bimetallic nanoparticles encapsulated in porous carbon have been prepared and utilized as effective electrocatalysts for both ORR and HER. The surface microstructure, crystal structure, as well as electronic charge states of the bimetallic particles encapsulated in porous carbon were studied by transmission electron microscopy (TEM), X-ray diffraction (XRD), and X-ray photoelectron spectroscopy (XPS), respectively. In the bimetallic Pd_xAg_{100-x} (x represents the initial atomic Pd ratio in PdAg alloys) series, the Pd₅₀Ag₅₀ sample exhibited the best performance, of which its ORR activity and long-term stability were superior to Pd/C in alkaline media along with its HER performance was comparable with Pd/C in acid solution. The study provides a reliable method for fabricating carbon substrate supported bimetallic alloys with good activity and robust stability toward ORR, HER and beyond.

Keywords: PdAg bimetallic nanoparticles; Porous carbon; Bifunctional electrocatalyst, Oxygen reduction reaction; Hydrogen evolution reaction

1. INTRODUCTION

To alleviate the global heavy reliance of fossil fuels and mitigate the associated environmental detrimental impacts, tremendous research efforts have been attracted to developing sustainable and high-efficiency energy storage and conversion devices, including proton exchange membrane fuel cells

(PEMFCs), rechargeable metal-air batteries and so on.[1-3] However, to commercialize these promising green energy devices, one of the key challenges is to develop efficient cathodic oxygen reduction reaction (ORR) catalysts to facilitate the sluggish reaction kinetics.[4, 5] Meanwhile, the hydrogen evolution reaction (HER) underpins a manifold of clean energy systems, and more importantly, HER has been widely regarded as a promising means to generate highly pure H₂, which has much higher energy density than conventional fuels and negligible negative environmental impacts.[6-8] Therefore, exploring efficient, cost-effective and durable bifunctional electrocatalysts to boost both ORR and HER performance is essential and imperative. To that end, great research efforts have been devoted to explore a variety of dual functional ORR and HER catalysts, including transition metal phosphides,[9] transition metal chalcogenides,[10, 11] metal carbide,[12] metal oxides,[13] graphene-based materials,[14] heteroatom doped carbon materials,[15, 16] metal-heteroatom-carbon systems.[17, 18] Although the above-mentioned catalysts have both fair ORR and HER dual functionalities, the most efficient catalysts for both ORR and HER are still Pt-based materials,[19, 20] especially in alkaline electrolyte in industry. Unfortunately, the high cost of Pt and its scarcity have significantly hampered the scalable commercialization. Furthermore, such Pt-based catalysts also suffer from undesired stability for long-term operations.[21, 22]

Compared with Pt, Pd has similar chemical properties but lower cost, and Pd can demonstrate effective electrocatalytic reactivity due to the formation of compact and stable palladium oxides.[5, 23] Note that, palladium nanoparticles with three dimensions in nanoscale, which can exhibit a large surface-to-volume ratio and abundant active centers, have been a prevailed choice of catalyst for various electrochemical reactions including ORR, HER, oxygen evolution reaction (OER) and so on.[24-26] For instance, Yan *et al.* prepared ultras-small Pd clusters embedded in porous carbon nanosheets, which exhibited outperformed ORR activity and stability to commercial Pd in alkaline media.[27] In another report, Yang *et al.* investigated peptide capped Pd nanoparticles for ORR in alkaline solution, and strong surface effects were noted between the peptide sequence and the catalytic performance.[28] Xu group developed a multi-site strategy for enhancing the HER activity on a nanoscale Pd surface in alkaline media, and bifunctional activities for both ORR and HER can be achieved.[29] Liu *et al.* developed a facile method to prepare Pd nanoparticle assemblies, which exhibited a low overpotential of 80 mV at a current density of 100 mA cm⁻² for HER and an onset potential of 0.926 V at 1600 rpm as well as a half-wave potential of 0.837 V for ORR in 0.1 M KOH.[30] To further enhance the intrinsic catalytic properties of Pd nanoparticles, one effective strategy is to alloy Pd with other metals to synergistically catalyze the electrochemical reactions. It is noteworthy that, carbon supported PdM alloys[24, 31] including PdFe,[32] PdMn,[32] PdCo,[33] PdNi,[34] PdCu,[35] PdAu,[36] PdMo,[37] and PdZn[31] have demonstrated at least comparable, if not superior, electrocatalytic performance with Pt/C for both ORR and HER in alkaline solution. The excellent electrochemical performance can be mainly attributed to the alloying effects, which include the ensemble effect and electronic effect.[38] Upon the introduction of a foreign metal, the configuration of the monometallic catalyst can be re-constructed and new catalytic active sites would be generated, which is the ensemble effect. The electronic effect is referring to that, there is electronic interaction between the two metals, and the heteroatom metal-to-metal bond is beneficial for activating the substrate and the catalyst.[38]

In this study, a series of Pd_xAg_{100-x} (x represents the initial atomic Pd ratio in PdAg alloys) alloy nanoparticles were prepared by using metal-organic framework of UIO-66 as precursor and employed as efficient electrocatalysts for both ORR and HER. The surface microstructure and electronic structure of the bimetallic nanoparticles were studied by TEM, XRD, XPS and so on. Among the series, the Pd₅₀Ag₅₀ sample showed superior ORR performance to the Pd/C catalyst in alkaline media, and it also demonstrated comparable activity and long term stability with Pd/C for HER in acid solution.

2. MATERIALS AND METHODS

2.1. Materials

Zirconium (IV) tetrachloride (ZrCl₄, 99%) was purchased from Aladdin chemical corporation (Shanghai, China). 2-Aminoterephthalic acid (C₈H₇NO₄, 98%), palladium (II) acetylacetonate (C₁₀H₁₄O₄Pd, 98%) and silver nitrate (AgNO₃, 99%) were acquired from Energy Chemicals (Shanghai, China). *N,N*-Dimethylformamide (DMF, 99.9%) and acetic acid (CH₃COOH, 99.8%) were bought from Damao Chemical Industry (Tianjin, China). 20 wt. % Pd/C was purchased from Alfa Aesar. Water was supplied by a Barnstead Water System (18.3 MΩ·cm). All chemicals were used as received.

2.2. Synthesis of Pd-doped UIO-66 (Pd-UIO-66)

For the preparation of Pd-UIO-66, a modified protocol of UIO-66 was adopted.[39] Firstly, 125 mg of zirconium tetrachloride (ZrCl₄), 135 mg of 2-aminoterephthalic acid and 15 mg of palladium (II) acetylacetonate were co-dissolved in 25 mL DMF, then 2 mL ice-cold acetic acid was added under stirring at room temperature for 10 mins, followed by ultrasonic treatment for 10 mins. The mixture was then transferred into a 50 mL hydrothermal reactor and heated for 10 h. Upon cooling down to room temperature, the collected solid was washed with DMF and anhydrous ethanol 3-5 times, and dried overnight in 40 °C. To increase the crystallinity and remove the residual organic linker, post annealing was conducted at 200 °C under Ar atmosphere for 2 h.

2.3. Synthesis of PdAg bimetallic nanoparticles encapsulated in porous carbon

In a typical synthesis, 150 mg of UIO-66 and 85 mg of silver nitrate was uniformly dispersed in 10 mL DMF under stirring with 400 r/min for 24 h. The formed precipitates were then collected, washed with DMF and anhydrous ethanol three times, and subsequently dried overnight in a vacuum of 40 °C. Then, 100 mg of the above solid was then loaded into a porcelain boat and pyrolyzed at 800 °C for 3 h with Ar/H₂ as the carrier gas and the heating rate of 5 °C /min. Finally, the calcined samples were etched in 2 M HF solution for 12 h to completely remove the ZrO₂ and Zr residues, and then rinsed with deionized water for multiple times and placed in a vacuum dry box overnight. For the other Pd_xAg_{100-x} samples with different Pd-to-Ag ratios, the whole metal amount was set fixed as 0.1 mol. The precursor

molar ratios of Pd-to-Ag was 83: 17, 75: 25, 50: 50, 25: 75, and 17: 83 for the sample of Pd₈₃Ag₁₇, Pd₇₅Ag₂₅, Pd₅₀Ag₅₀, Pd₂₅Ag₇₅, and Pd₁₇Ag₈₃, respectively.

2.4. Characterizations

The surface structures and morphologies of the samples were observed via field emission scanning electron microscopy (SEM, Hitachi S-4800) and high-resolution transmission electron microscopy (HR-TEM, Tecnai G2 F30). X-ray diffraction (XRD) patterns in the Bragg's angle (2θ) range of 10° - 90° were acquired using a Bruker D8 diffractometer with Cu K_α radiation ($\lambda = 0.1541$ nm). TEM graphs were obtained with a high-resolution transmission electron microscope (JEOL JEM-2010), where the samples were prepared by dropwise casting a catalyst dispersion directly onto a copper grid coated with a holey carbon film. X-ray photoelectron spectroscopy (XPS) analysis was performed with a VG MultiLab 2000 instrument with a monochromatic Al K X-ray source (Thermo VG Scientific).

2.5. Electrochemical measurements

For ORR test, the measurements were conducted with a CHI 750E electrochemical workstation (CH Instruments Inc.) in a 0.1 M KOH aqueous solution at ambient temperature. Platinum electrode and Ag/AgCl electrode were employed as the counter electrode and reference electrode respectively. The catalyst modified rotating disk electrode (RDE) from Pine Instruments was employed as the working electrode. The working electrode is polished by 0.3 μm alumina powder. To prepare the catalyst ink, 5 mg of catalyst was dispersed in 1 mL mixed solution, which contained 500 μL absolute ethanol, 450 μL deionized water and 50 μL Nafion (5 wt.%, Aldrich). The catalyst ink (10 μL) was loaded on the surface of electrode, and the loading amount was about 50 μg . In all the tests, the potential was referred to a reversible hydrogen electrode (RHE): $E_{(RHE)} = E_{(Ag/AgCl)} + (0.197 + 0.0591 * \text{pH})$. Before ORR test, all the electrodes were activated by cyclic voltammetric scans for 50 times in N_2 -saturated 0.1 M KOH solution at a scan rate of 50 mV s^{-1} in the potential range of 0 - 1.0 V. For HER test, the operations were quite similar with ORR. A three-electrode device was employed for the HER measurements, in which the carbon rod and Hg/ Hg_2Cl_2 electrode were used as the counter electrode and reference electrode, and the glassy carbon electrode (GCE) was used as the working electrode in 0.5 M H_2SO_4 solution, $E_{(RHE)} = E_{(SCE)} + (0.24 + 0.0591 * \text{pH})$. All the potentials were referred to the reversible hydrogen electrode without correcting the ohmic potential loss in the solution.

3. RESULTS AND DISCUSSIONS

3.1. TEM analysis of the Pd₅₀Ag₅₀ sample

Firstly, Pd-doped metal-organic framework of UIO-66 (Pd-UIO-66) was prepared by hydrothermal method. Silver ions were then introduced by physical adsorption, and the sample was calcined under reductive gas atmosphere of Ar- H_2 . The products were pickled by HF and bimetallic

$\text{Pd}_x\text{Ag}_{100-x}$ nanoparticles encapsulated in porous carbon were obtained. The surface microstructure of the $\text{Pd}_{50}\text{Ag}_{50}$ sample was then studied by electron microscope techniques. From **Figure 1a**, spherical particles cluster together can be clearly observed with various tiny pores onto the surface. Such pore structure with high surface area can probably provide abundant active sites for electrocatalysis. The emergence of the mesopores is presumably being produced during the pickling process. The further lattice parameter information was acquired by HR-TEM. **Figure 1b** shows that the lattice spacing of $\text{Pd}_{50}\text{Ag}_{50}$ is 0.231 nm and 0.199 nm, which corresponds well with the 111 and 200 crystal planes of the PdAg alloy, respectively. It should be noted that, the lattice spacing of the 200 and 111 crystal plane of $\text{Pd}_{50}\text{Ag}_{50}$ alloy is in the between pure Ag and pure Pd, implying the formation of the PdAg alloys.[39, 40] According to the EDX results (**Figure 1c**), the Pd/Ag atomic ratio was 16.55/17.06, in good accordance with 1/1. In addition, **Figure 1d-g** show the mapping images of the Pd, Ag and C elements, and one can see that all the elements are uniformly distributed, further confirming PdAg alloyed nanoparticles encapsulated in porous carbon have been successfully acquired.

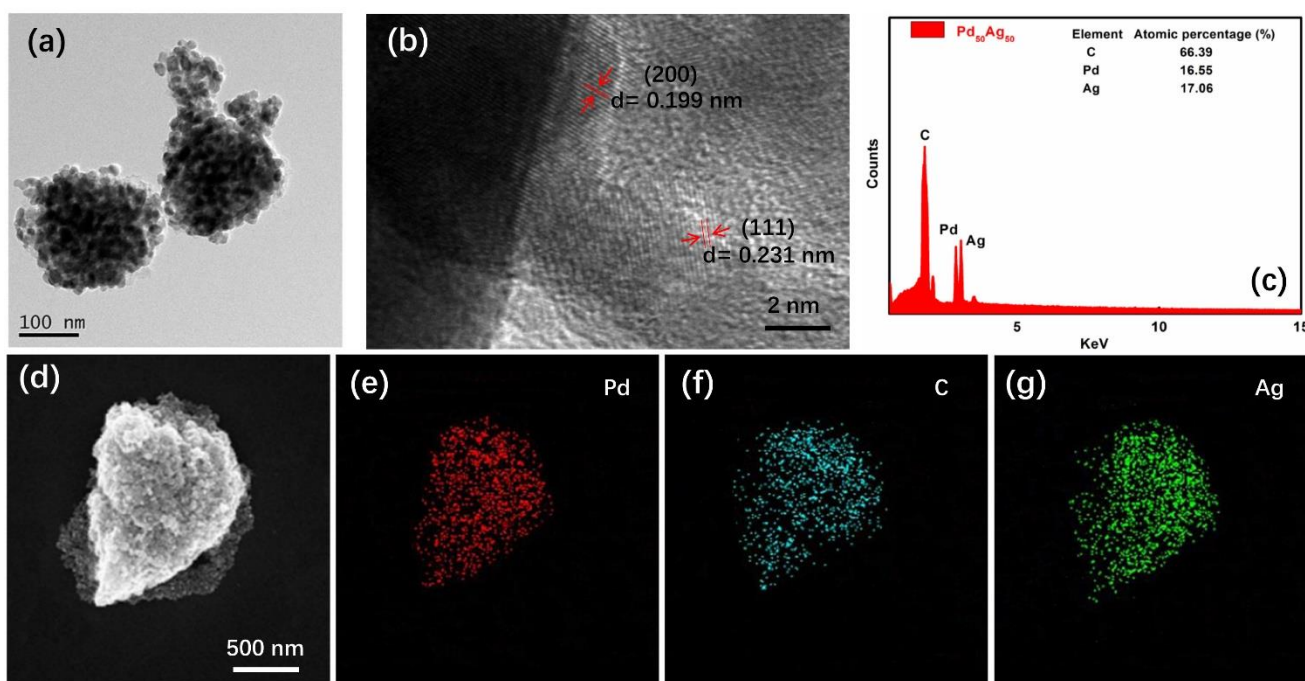


Figure 1. Representative (a) TEM and (b) HR-TEM image of $\text{Pd}_{50}\text{Ag}_{50}$. (c) Energy-disperse X-ray spectrum (EDX) taken on the selected area of the $\text{Pd}_{50}\text{Ag}_{50}$ sample. (d) SEM image of the $\text{Pd}_{50}\text{Ag}_{50}$ sample, and corresponding elemental mapping of (e) Pd, (f) C, (g) Ag.

3.2. XRD and XPS analysis of the $\text{Pd}_x\text{Ag}_{100-x}$ series

The crystal phase information profile of the series was subsequently acquired by XRD and shown in **Figure 2a**. The peak position of the PdAg nanoparticles is well-consistent with the standard PDF cards of Pd and Ag. It is worth noting that with the increase of the atomic ratio of Pd-to-Ag, the intensity of the corresponding 2θ peak gradually changed correspondingly. For the $\text{Pd}_{50}\text{Ag}_{50}$ sample, both the

XRD peak of Pd and Ag appeared with somewhat offset, indicating well-defined bimetallic alloys were obtained.[36, 41] Then the electronic structure of the samples was probed by XPS measurement. The core-level XPS spectra of the Ag3d electrons for all the samples are illustrated in **Figure 2b**. The broad peak can be fitted into two defined peaks, which are attributable to the Ag3d_{5/2} and Ag3d_{3/2} electrons, respectively. For Ag₈₃Pd₁₇, the two peaks with binding energies at 368.2 eV and 374.1 eV are in good accordance with Ag(0).[42] With the increasing of Ag ratio in the alloys, the broad peak of the Ag3d electrons gradually became much sharper, and the background noise also got weakened. Interestingly, there is binding energy downshift with the increasing of Ag ratio in the Pd_xAg_{100-x} series. Compared with Pd₁₇Ag₈₃, the binding energy of the Ag3d electrons in Pd₅₀Ag₅₀ increased, indicating there is electron transfer from Ag atoms to Pd atoms. Such phenomenon was further confirmed in the XPS spectra of the Pd3d_{5/2} electrons (**Figure 2c**). Compared with Pd₈₃Ag₁₇, the binding energy of the Pd3d_{5/2} electrons in Pd₅₀Ag₅₀ is about 0.68 eV lower, suggesting that Pd elements are gaining electrons. Note that, previous studies have demonstrated that such electron transfer behaviors are favorable for facilitating the electrocatalytic reaction kinetics hence promoting the catalytic performance.[41, 43]

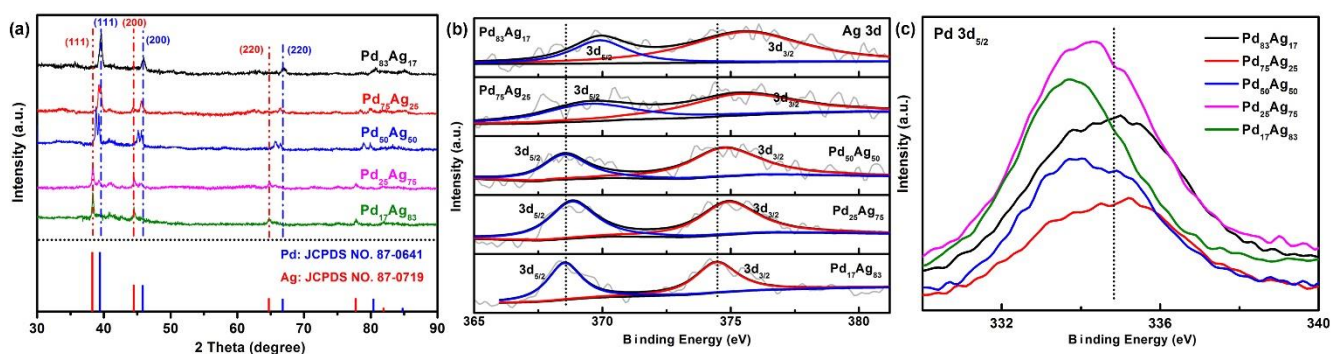


Figure 2. (a) XRD patterns of the Pd_xAg_{100-x} samples. (b) The core-level Ag 3d XPS spectra and (c) The core-level Pd 3d_{5/2} XPS spectra of the Pd₈₃Ag₁₇, Pd₇₅Ag₂₅, Pd₅₀Ag₅₀, Pd₂₅Ag₇₅, and Pd₁₇Ag₈₃ samples.

3.3. Electrocatalytic performance of the Pd_xAg_{100-x} series for ORR in alkaline media

Table 1. The ORR and HER activity comparison of the Pd_xAg_{100-x} series and Pd/C.

Sample	ORR (0.1 M KOH)			HER (0.5 M H ₂ SO ₄)
	E _{1/2} (V vs. RHE)	n value	Diffusion-limiting current (mA cm ⁻²)	Overpotential @ 10 mA cm ⁻² (mV)
Pd ₈₃ Ag ₁₇	0.78	/	3.6	148
Pd ₇₅ Ag ₂₅	0.75	/	4.5	123
Pd ₅₀ Ag ₅₀	0.81	3.7-3.9	4.7	97
Pd ₂₅ Ag ₇₅	0.73	/	3.9	235
Pd ₁₇ Ag ₈₃	0.77	/	4.2	191
Pd/C	0.79	3.6-3.8	4.0	50

The as-prepared samples were then subjected to the electrochemical test toward ORR by RDE in a 0.1 M O₂-saturated KOH solution. The ORR performance of the samples is summarized in **Table 1**. As shown in **Figure 3a**, a reduction peak ranging from 0.50 V to 0.90 V is shown in the CV curve, indicating that all the samples had effective ORR activities.

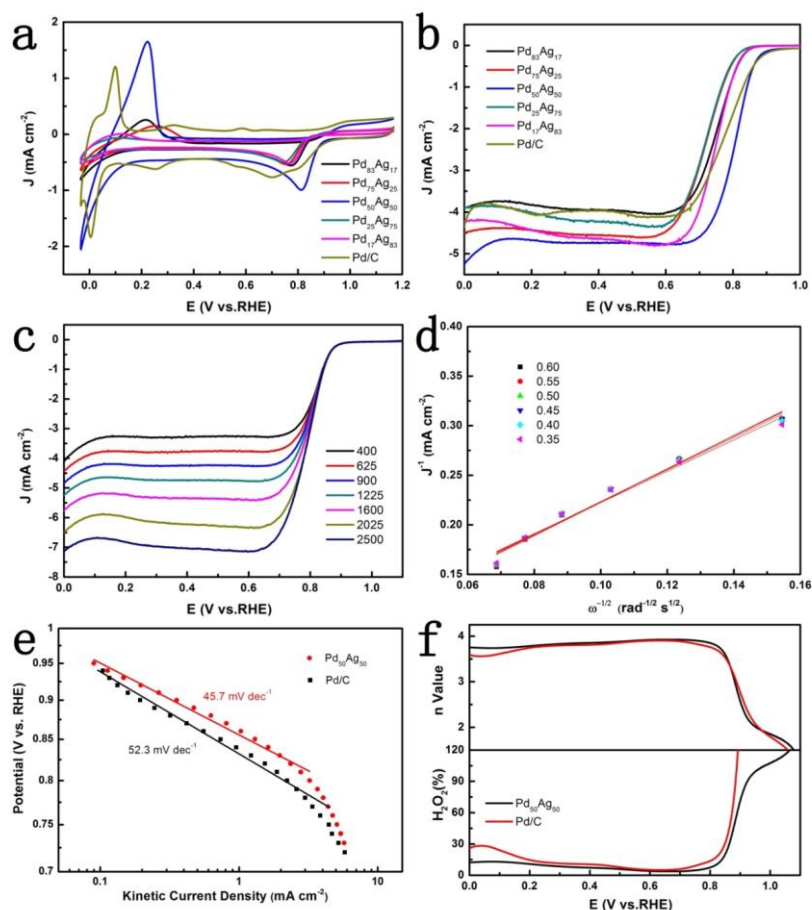


Figure 3. (a) The CV curves of Pd₈₃Ag₁₇, Pd₇₅Ag₂₅, Pd₅₀Ag₅₀, Pd₂₅Ag₇₅, Pd₁₇Ag₈₃, and Pd/C in O₂-saturated 0.1 M KOH solution (b) The LSV curves of Pd₈₃Ag₁₇, Pd₇₅Ag₂₅, Pd₅₀Ag₅₀, Pd₂₅Ag₇₅, Pd₁₇Ag₈₃, and Pd/C in an O₂-saturated 0.1 M KOH solution at a sweep speed of 10 mV s⁻¹ and electrode rotation rate of 1600 rpm. (c) The LSV curves for Pd₅₀Ag₅₀ at a rotation rate of 400 - 2500 rpm. (d) The corresponding K-L plot of Pd₅₀Ag₅₀. (e) The Tafel slope values at low overpotential regions for Pd₅₀Ag₅₀ and Pd/C. (f) Plots of H₂O₂ yield and number of electron transfer (n) of a glassy carbon electrode modified with Pd₅₀Ag₅₀ and Pd/C at a rotation rate of 1600 rpm.

The cathodic peak potential can be estimated as 0.78 V, 0.75 V, 0.81 V, 0.73 V, 0.77 V, and 0.79 V for Pd₈₃Ag₁₇, Pd₇₅Ag₂₅, Pd₅₀Ag₅₀, Pd₂₅Ag₇₅, Pd₁₇Ag₈₃, and Pd/C, respectively. Among all the samples, Pd₅₀Ag₅₀ showed the most positive cathodic peak potential and the largest cathodic peak current density, indicating it had the best oxygen reduction performance. To further study the ORR activity, RRDE measurement was then carried out. As presented in **Figure 3b**, the linear sweep voltammetric (LSV) curves clearly show that the half-wave potential and diffusion-limiting current density changed drastically with the change of the atomic ratio of Pd and Ag. Pd₅₀Ag₅₀ had the maximal half-wave

potential value of 0.81 V, superior to that of Pd/C. In addition, the diffusion-limiting current densities of Pd₇₅Ag₂₅, Pd₅₀Ag₅₀, and Pd₁₇Ag₈₃ are higher than that Pd/C (**Table 1**). As Pd₅₀Ag₅₀ showed the best activity in the series, its ORR performance was further studied and compared with the commercial Pd/C catalyst. As depicted in **Figure 3c**, the current density increases with the increase of electrode rotation speed. The corresponding Koutecky-Levich (K-L) plots are shown in **Figure 3d**. In the potential range of 0.35 to 0.60 V, the reaction has a good linear relationship and the slope is nearly identical, indicating that the reaction has a first-order kinetic relationship with regard to the concentration of the dissolved oxygen in the solution. To disclose the reaction kinetics, the Tafel plots of Pd₅₀Ag₅₀ and Pd/C were drawn where the Tafel slope values can be extrapolated (**Figure 3e**). The Tafel slope value of Pd₅₀Ag₅₀ is 45.7 mV dec⁻¹, smaller than that of Pd/C (52.3 mV dec⁻¹), indicating that Pd₅₀Ag₅₀ adopted a faster reaction kinetics than Pd/C. Furthermore, the electron transfer number (n) and hydrogen peroxide (H₂O₂) yield of Pd₅₀Ag₅₀ were calculated on the basis of RRDE voltammetric curves and compared with Pd/C. As illustrated in **Figure 3f**, Pd₅₀Ag₅₀ exhibited the hydrogen peroxide yield of 4.2-14.5 % in the potential range of 0-0.8 V, lower than that of Pd/C (4.3-29.8 %), while correspondingly, it possessed an electron transfer number of 3.7-3.9, higher than that of Pd/C (3.6-3.8). The electron transfer number is also close to 4, suggesting a highly-efficient 4-electron transfer pathway was adopted for Pd₅₀Ag₅₀. [44, 45]

3.4. Long term durability of Pd₅₀Ag₅₀ compared with Pd/C for ORR in alkaline media

Subsequently, chronoamperometric measurements were first carried out to evaluate the long-term durability of Pd₅₀Ag₅₀ in comparison with Pd/C. As presented in **Figure 4a**, after continuous operation for more than 20,000 s, the cathodic current of the Pd/C catalyst was 14.4% lower than its initial value. However, under the same conditions, the Pd₅₀Ag₅₀ cathode current maintained about 91.8% of the initial value with only 8.2% loss. The much smaller current attenuation indicates that Pd₅₀Ag₅₀ had higher long term durability than Pd/C. Furthermore, the stability of Pd₅₀Ag₅₀ was confirmed by the accelerated durability test (ADT) in O₂-saturated 0.1 M KOH solution from the potential range of 0.6 V to 1.0 V. As shown in **Figure 4b**, after 2500 cycles of potential scan, the half-wave potential of Pd₅₀Ag₅₀ had a negative shift of only 4 mV, while the potential shift of Pd/C with a value of 18 mV is much larger (**Figure 4c**), further proving that Pd₅₀Ag₅₀ had an outperformed durability over the Pd/C catalyst.

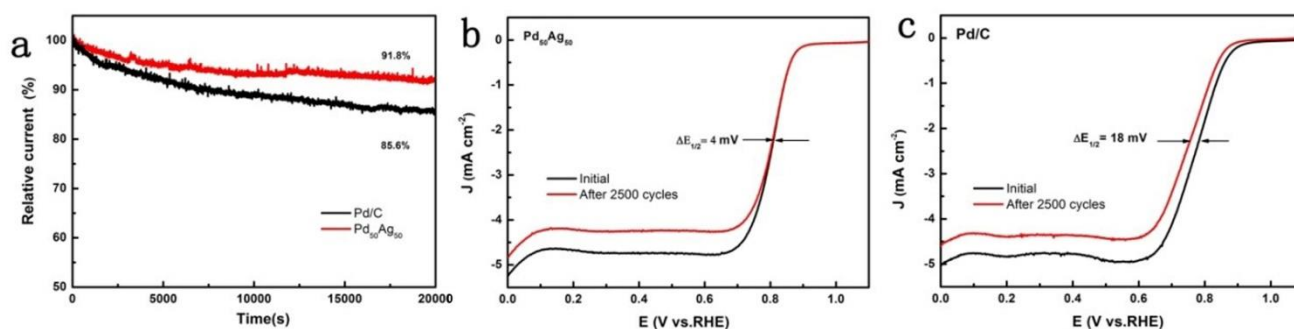


Figure 4. (a) Chronoamperometric graph of Pd₅₀Ag₅₀ and Pd/C at 0.5 V for 20,000 s. The LSV curves of (b) Pd₅₀Ag₅₀ (c) Pd/C before and after 2500 cycles of potential scan. All measurements were performed in oxygen-saturated 0.1 M KOH solution.

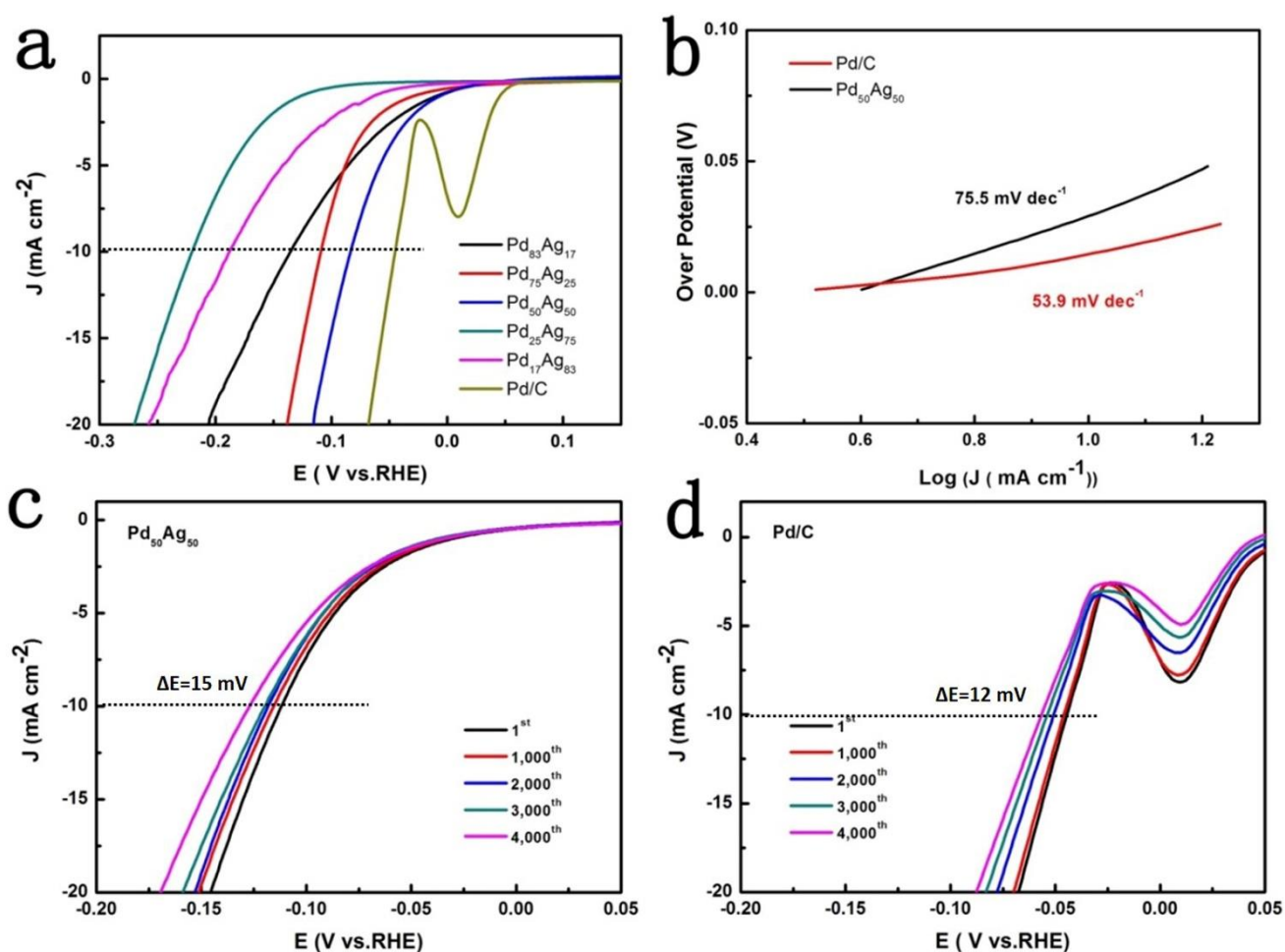
3.5. Electrocatalytic performance of the Pd_xAg_{100-x} series for HER in acid solution

Figure 5. (a) Polarization curves of the samples for HER at a scan rate of 10 mV s⁻¹. (b) Tafel plots of Pd₅₀Ag₅₀ and Pd/C. (c) Polarization curves of Pd₅₀Ag₅₀, (d) Pd/C recorded at the 1st scan and after 4000th continuous CV cycles at a scan rate of 100 mV s⁻¹. All the tests were conducted in 0.5 M H₂SO₄.

The HER properties of the samples were finally evaluated by GCE in a three-electrode device in acid media and the performance comparison summary is also compiled in **Table 1**. **Figure 5a** shows the LSV curves of the Pd_xAg_{100-x} series at a scan speed of 10 mV s⁻¹ compared to the Pd/C catalyst in 0.5 M H₂SO₄. To afford a current density of 10 mA cm⁻², the overpotential of Pd₈₃Ag₁₇, Pd₇₅Ag₂₅, Pd₅₀Ag₅₀, Pd₂₅Ag₇₅, Pd₁₇Ag₈₃, and Pd/C is 148 mV, 123 mV, 97 mV, 235 mV, 191 mV, and 50 mV, respectively. It indicates that Pd₅₀Ag₅₀ had the best HER activity in the series, and its HER performance is also approaching to Pd/C. The reaction kinetics of Pd₅₀Ag₅₀ was then elucidated and compared with Pd/C. **Figure 5b** shows the Tafel plots of Pd₅₀Ag₅₀ and Pd/C, and the Tafel slope values of Pd₅₀Ag₅₀ and Pd/C are determined as 75.5 mV dec⁻¹ and 53.9 mV dec⁻¹, respectively, indicating that Pd₅₀Ag₅₀ had the similar hydrogen evolution kinetics as the Pd/C catalyst. Finally, the long-term stability of Pd₅₀Ag₅₀ was evaluated and compared with Pd/C by ADTs in 0.5 M H₂SO₄. [46] As illustrated in **Figure 5c**, after 4000 cycles of potential scans, to afford a current density of 10 mA cm⁻², the overpotential of Pd₅₀Ag₅₀ shifted negatively about 15 mV, quite close to that of Pd/C (12 mV, **Figure 5d**). The ADT test proved that Pd₅₀Ag₅₀ had excellent long term stability comparable with Pd/C for HER in acid solution.

Table 2. The ORR and HER performance of Pd₅₀Ag₅₀ compared with the recently reported palladium-based alloys.

Sample	ORR (0.1 M KOH)		HER (0.5 M H ₂ SO ₄)		Reference
	<i>n</i> value	<i>E</i> _{1/2} (V vs. RHE)	Overpotential @10 mA cm ⁻² (mV)		
Pd ₅₀ Ag ₅₀	3.7-3.9	0.81	97		This work
Pd/HSAG	3.4-3.5	0.80	63		[47]
PdNi/NG	-	0.70	-		[48]
PdNiSn/NG	-	0.76	-		[48]
Pd ₄₀ Cu ₆₀ /C	-	-	189		[49]
Pd- <i>g</i> -C ₃ N ₄	-	0.70	-		[50]
Au ₆₇ Pd ₃₃ /CNs	3.8-3.9	0.81	-		[36]

It is interesting to note that, the ORR and HER performance of the Pd₅₀Ag₅₀ sample is comparable with even superior to the recently reported Pd-based nanostructured catalysts, as summarized in **Table 2**. For instance, for ORR in 0.1 M KOH, the electron transfer number of Pd₅₀Ag₅₀ was 3.7-3.9, close to that of Au₆₇Pd₃₃/CNs,[36] but higher than that of Pd/HSAG.[47] In addition, the half-wave potential of Pd₅₀Ag₅₀ was 0.81 V, same with that of Au₆₇Pd₃₃/CNs,[36] but more positive than Pd/HSAG,[47] PdNi/NG,[48] PdNiSn/NG,[48] and Pd-*g*-C₃N₄.[50] Furthermore, Pd₅₀Ag₅₀ also exhibited superior HER reactivity to Pd₄₀Cu₆₀/C,[49] as evidenced by the much lower overpotential at the current density of 10 mA cm⁻² in 0.5 M H₂SO₄. Such excellent performance of the Pd₅₀Ag₅₀ sample can be probably attributed to its PdAg alloying effects, as manifested by the electron transfer behaviours observed in the XPS results.

4. CONCLUSIONS

In summary, a series of bimetallic Pd_xAg_{100-x} alloy nanoparticles encapsulated in porous carbon were prepared as dual functional electrocatalysts for both ORR and HER. In alkaline media, the Pd₅₀Ag₅₀ sample showed the best electrocatalytic performance in the series, in which its ORR activity and long-term stability are superior to the Pd/C catalyst in alkaline media, along with its HER activity and durability are close to Pd/C in acid solution. The remarkable bifunctional electrocatalytic activity of Pd₅₀Ag₅₀ can be attributed to the synergistic catalytic effects from the bimetallic PdAg alloys, as evidenced by the electron transfer behaviors observed in XPS. This study can pave a path for preparing carbon substrate supported non-Pt bimetallic nanomaterials as efficient electrocatalysts toward ORR, HER and beyond.

ACKNOWLEDGEMENTS

W. H. thanks the funding support from Science and Technology Program of Chongqing Teaching Committee (No. KJ1604301), Z. H. T acknowledges financial support from Guangdong Innovative and Entrepreneurial Research Team Program (No. 2014ZT05N200).

References

1. M. K. Debe, *Nature*, 486 (2012) 43.
2. Z. Ding, Z. Tang, L. Li, K. Wang, W. Wu, X. Chen, X. Wu, S. Chen, *Inorg. Chem. Front.*, 5 (2018) 2425.
3. K. Wang, W. Wu, Z. Tang, L. Li, S. Chen, N. M. Bedford, *ACS Appl. Mater. Interfaces*, 11 (2019) 4983.
4. D. Gu, Y. Zhou, R. Ma, F. Wang, Q. Liu, J. Wang, *Nano-Micro Lett.*, 10 (2017) 29.
5. M. Shao, Q. Chang, J.-P. Dodelet, R. Chenitz, *Chem. Rev.*, 116 (2016) 3594.
6. J. Wei, M. Zhou, A. Long, Y. Xue, H. Liao, C. Wei, J. Z. Xu, *Nano-Micro Lett.*, 10 (2018) 75.
7. J. Wang, F. Xu, H. Jin, Y. Chen, Y. Wang, *Adv. Mater.*, 29 (2017) 1605838.
8. A. Saeedmanesh, M. M. Kinnon, J. Brouwer, *Curr. Opin. Electrochem.*, 12 (2018) 166.
9. H. Tabassum, W. Guo, W. Meng, A. Mahmood, R. Zhao, Q. Wang, R. Zou, *Adv. Energy Mater.*, 7 (2017) 1601671.
10. Y. Yan, B. Y. Xia, Z. C. Xu, X. Wang, *ACS Catal.*, 4 (2014) 1693.
11. Z. Qian, Y. Chen, Z. Tang, Z. Liu, X. Wang, Y. Tian, W. Gao, *Nano-Micro Lett.*, 11 (2019) 28.
12. J.-S. Li, Y. Wang, C.-H. Liu, S.-L. Li, Y.-G. Wang, L.-Z. Dong, Z.-H. Dai, Y.-F. Li, Y.-Q. Lan, *Nat. Commun.*, 7 (2016) 11204.
13. T. Ma, C. Li, X. Chen, F. Cheng, J. Chen, *Inorg. Chem. Front.*, 4 (2017) 1628.
14. M. Liu, R. Zhang, W. Chen, *Chem. Rev.*, 114 (2014) 5117.
15. R. Li, Z. Wei, X. Gou, *ACS Catal.*, 5 (2015) 4133.
16. K. Gong, F. Du, Z. Xia, M. Durstock, L. Dai, *Science*, 323 (2009) 760.
17. W. Niu, L. Li, X. Liu, N. Wang, J. Liu, W. Zhou, Z. Tang, S. Chen, *J. Am. Chem. Soc.*, 137 (2015) 5555.
18. J. Yin, Q. Fan, Y. Li, F. Cheng, P. Zhou, P. Xi, S. Sun, *J. Am. Chem. Soc.*, 138 (2016) 14546.
19. X. Huang, Z. Zhao, L. Cao, Y. Chen, E. Zhu, Z. Lin, M. Li, A. Yan, A. Zettl, Y. M. Wang, X. Duan, T. Mueller, Y. Huang, *Science*, 348 (2015) 1230.
20. L. Wang, Z. Tang, W. Yan, Q. Wang, H. Yang, S. Chen, *J. Power Sources*, 343 (2017) 458.
21. C. Wang, N. M. Markovic, V. R. Stamenkovic, *ACS Catal.*, 2 (2012) 891.
22. D. Strmcnik, P. P. Lopes, B. Genorio, V. R. Stamenkovic, N. M. Markovic, *Nano Energy*, 29 (2016) 29.
23. M. Shao, J. Odell, M. Humbert, T. Yu, Y. Xia, *J. Phys. Chem. C*, 117 (2013) 4172.
24. L. Zhang, Q. Chang, H. Chen, M. Shao, *Nano Energy*, 29 (2016) 198.
25. E. Antolini, *Energy Environ. Sci.*, 2 (2009) 915.
26. T. Li, Y. Chen, Z. Tang, Z. Liu, C. Wang, *Electrochim. Acta*, 307 (2019) 403.
27. W. Yan, Z. Tang, L. Li, L. Wang, H. Yang, Q. Wang, W. Wu, S. Chen, *ChemElectroChem*, 4 (2017) 1349.
28. H. Yang, Z. Tang, W. Yan, L. Wang, Q. Wang, Y. Zhang, Z. Liu, S. Chen, *J. Alloys. Compd.*, 702 (2017) 146.
29. H. Liao, C. Wei, J. Wang, A. Fisher, T. Sritharan, Z. Feng, Z. J. Xu, *Adv. Energy Mater.*, 7 (2017) 1701129.
30. S. Liu, X. Mu, H. Duan, C. Chen, H. Zhang, *Eur. J. Inorg. Chem.*, 2017 (2017) 535.
31. G. Bampos, S. Bebelis, D. I. Kondarides, X. Verykios, *Top. Catal.*, 60 (2017) 1260.
32. Y. Holade, R. G. da Silva, K. Servat, T. W. Napporn, C. Canaff, A. R. de Andrade, K. B. Kokoh, *J. Mater. Chem. A*, 4 (2016) 8337.
33. H. Yang, Z. Tang, K. Wang, W. Wu, Y. Chen, Z. Ding, Z. Liu, S. Chen, *J. Colloid Interf. Sci.*, 528 (2018) 18.
34. Y. Li, S. Lin, X. Ren, H. Mi, P. Zhang, L. Sun, L. Deng, Y. Gao, *Electrochim. Acta*, 253 (2017) 445.
35. J. Wu, S. Shan, J. Luo, P. Joseph, V. Petkov, C.-J. Zhong, *ACS Appl. Mater. Interfaces*, 7 (2015)

25906.

36. W. Yan, Z. Tang, L. Wang, Q. Wang, H. Yang, S. Chen, *Int. J. Hydrogen Energy*, 42 (2017) 218.
37. W. Yan, W. Wu, K. Wang, Z. Tang, S. Chen, *Int. J. Hydrogen Energy*, 43 (2018) 17132.
38. K. D. Gilroy, A. Ruditskiy, H.-C. Peng, D. Qin, Y. Xia, *Chem. Rev.*, 116 (2016) 10414.
39. L. Chen, B. Huang, X. Qiu, X. Wang, R. Luque, Y. Li, *Chem. Sci.*, 7 (2016) 228.
40. L. Huang, J. Yang, M. Wu, Z. Shi, Z. Lin, X. Kang, S. Chen, *J. Power Sources*, 398 (2018) 201.
41. D. Li, Z. Tang, S. Chen, Y. Tian, X. Wang, *ChemCatChem*, 9 (2017) 2980.
42. X. Jiang, Y. Xiong, Y. Wang, J. Wang, N. Li, J. Zhou, G. Fu, D. Sun, Y. Tang, *J. Mater. Chem. A*, 7 (2019) 5248.
43. Z. Zong, K. Xu, D. Li, Z. Tang, W. He, Z. Liu, X. Wang, Y. Tian, *J. Catal.*, 361 (2018) 168.
44. L. Wang, Z. Tang, W. Yan, H. Yang, Q. Wang, S. Chen, *ACS Appl. Mater. Interfaces*, 8 (2016) 20635.
45. Q. Wang, L. Wang, Z. Tang, F. Wang, W. Yan, H. Yang, W. Zhou, L. Li, X. Kang, S. Chen, *Nanoscale*, 8 (2016) 6629.
46. T. Li, Z. Tang, K. Wang, W. Wu, S. Chen, C. Wang, *Int. J. Hydrogen Energy*, 43 (2018) 4932.
47. M. Nunes, D. M. Fernandes, M. V. Morales, I. Rodríguez-Ramos, A. Guerrero-Ruiz, C. Freire, *Catal. Today*, (2019), 10.1016/j.cattod.2019.04.043.
48. L. Sun, B. Liao, X. Ren, Y. Li, P. Zhang, L. Deng, Y. Gao, *Electrochim. Acta*, 235 (2017) 543.
49. X. Zhang, D. Wu, D. Cheng, *Electrochim. Acta*, 246 (2017) 572.
50. S. K. Konda, M. Amiri, A. Chen, *J. Phys. Chem. C*, 120 (2016) 14467.

© 2019 The Authors. Published by ESG (www.electrochemsci.org). This article is an open access article distributed under the terms and conditions of the Creative Commons Attribution license (<http://creativecommons.org/licenses/by/4.0/>).